

Reversible Structural Evolution of NiCoO_xH_y during the Oxygen Evolution Reaction and Identification of the Catalytically Active Phase

Zhu Chen,^{†,||} Li Cai,^{‡,||} Xiaofang Yang,[†] Coleman Kronawitter,[§] Liejin Guo,^{‡,||} Shaohua Shen,^{*,‡} and Bruce E. Koel^{*,†,||}

[†]Department of Chemical and Biological Engineering, Princeton University, Princeton, New Jersey 08540, United States

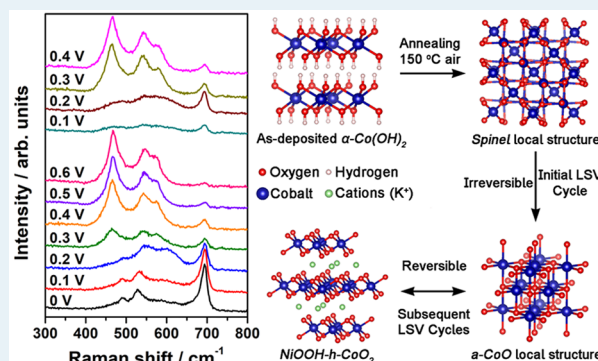
[‡]International Research Centre of Renewable Energy, State Key Laboratory of Multiphase Flow in Power Engineering, Xi'an Jiaotong University, Shaanxi 710049, PR China

[§]Department of Chemical and Biological Engineering, University of California, Davis, California 95616, United States

Supporting Information

ABSTRACT: Operando Raman spectroscopy and electrochemical techniques were used during the oxygen evolution reaction to identify the composition and local structure of electrodeposited CoO_xH_y and NiCoO_xH_y catalyst films. Before evaluation, the electrodeposited samples were subjected to a variety of thermal and electrochemical conditioning procedures, which generated unique initial catalyst structures and crystallinities. During oxygen evolution, Ni-modified CoO_xH_y films having lower initial crystallinity underwent substantial structural evolution that began with an irreversible transformation of a spinel local structure to an amorphous CoO structure at low anodic potentials (0.2 V vs Ag/AgCl). Increasing anodic polarization to greater than 0.3 V vs Ag/AgCl facilitated additional structural conversion from the amorphous CoO structure to a complex phase best described as an amalgamation of NiOOH and layered CoO_2 motifs (NiOOH-h-CoO_2) under elevated oxygen evolution rates. The formation of this NiOOH-h-CoO_2 active structure was correlated with improved OER activity, which at 0.35 V overpotential is 100% greater than that of the catalyst where Ni was coordinated in a spinel structure. Independent of the initial cobalt oxide structure, the same NiOOH-h-CoO_2 structure was formed during oxygen evolution, which suggests the active phase identified herein could be the universally active structure for NiCoO_xH_y materials.

KEYWORDS: operando Raman spectroscopy, oxygen evolution reaction, reversible structural evolution, spinel structure, amorphous cobalt oxide, layered delafossite, cobalt oxyhydroxide, Ni incorporation



INTRODUCTION

The oxygen evolution reaction (OER) is a major cause of energy losses in a number of emergent technologies such as rechargeable metal-air batteries,^{1,2} water splitting devices,^{3–6} and unitized regenerative fuel cells.⁷ The low energy efficiencies of OER are the results of its sluggish reaction kinetics and large overpotentials. Completing one OER cycle requires four electron transfers involving multiple surface intermediates, which when combined with the high irreversibility of OER leads to sluggish kinetics, large overpotential, and ultimately low device efficiency.⁸ Catalysts can be used to overcome these obstacles, but for large-scale applications they must be active, stable, and affordable. The most active OER catalysts to date are ruthenium oxide (RuO_2) and iridium oxide (IrO_2). However, RuO_2 is not stable due to catalyst dissolution into the electrolyte via Ru^{8+} formation during reaction,^{9,10} and IrO_2 suffers from low elemental Ir abundance. The latter limits the

practical application of IrO_2 catalyst despite its high activity and better stability compared to RuO_2 .^{11–14} Alternatives to these precious metal catalysts are transition-metal oxides (TMO), which have low costs, great elemental abundance, and have demonstrated excellent OER activities. In particular, TMO based on Fe, Ni, and Co are highly active for OER in alkaline conditions, according to comprehensive benchmarking studies from the Jaramillo^{15–17} and Boettcher groups.^{18,19}

In light of their excellent OER performance, significant research efforts have focused on elucidating the structure–activity correlations of TMO catalysts that contain Fe, Ni, and Co. However, this effort is hindered by difficulties associated with an accurate determination of active catalyst structures

Received: September 19, 2017

Revised: November 20, 2017

Published: December 8, 2017

based on their characterization only before and after OER. In contrast, *operando* techniques can provide information on catalyst structure, composition, and surface species during catalytic turnover, and such techniques have been applied to a number of TMO catalysts.^{20–27} For example, using *operando* time-resolved FTIR, Zhang et al. identified critical reaction intermediates (i.e., surface superoxides) on Co₃O₄ nanoparticles during OER. These authors proposed a dual-site OER mechanism on Co₃O₄, which includes a kinetically fast site consisting of two Co³⁺–OH surface species bridged by an O atom, and a slow site associated with isolated Co⁴⁺=O surface species.²⁸ Friebe et al. implemented *operando* X-ray absorption spectroscopy (XAS) to characterize the chemical states and the local structures of Ni_{1–x}Fe_xOOH. These authors discovered an active structure motif that consisted of Fe³⁺ in an octahedral site with unusually short Fe³⁺–O bond distances, which resulted in near-optimal adsorption energies of OER intermediates and reduced overpotentials at these Fe sites.²⁹

In studies reported herein, we investigated the influence of Ni incorporation on the catalyst activity and structural evolution of substoichiometric cobalt (oxy)hydroxide (CoO_xH_y) during OER. Pure and nickel-modified cobalt oxide catalysts such as Co₃O₄,^{30–32} CoOOH,^{33,34} and NiCo hydroxides³⁵ have demonstrated excellent OER activities and attracted considerable research interest. However, understanding the structure–activity correlations in these catalysts is difficult due to the dynamic structural evolutions that occur during OER. For example, layered double hydroxides of Co (α - and β -Co(OH)₂) have been shown to undergo structural conversion under different applied potentials and pH.³⁶ Even for highly crystalline Co₃O₄ catalysts, prolonged exposure to strong alkaline conditions under large anodic potentials can lead to surface amorphization and a decrease in OER activity.^{24,37} As a result, the activity and stability of cobalt oxide OER catalysts depend critically on the structural changes that occur during reaction. *Operando* Raman spectroscopy is excellent for probing the structural evolution of TMO catalysts during OER. Using this technique, the conversion of NiO and Co₃O₄ to NiOOH and CoO(OH), respectively, was observed under anodic polarization in alkaline conditions.^{22,24} With the same approach, Louie and Bell also observed an increase in the Ni(OH)₂/NiOOH redox potential with Fe incorporation into the catalyst, which increased OER activity.²³ Despite its great relevance, *operando* Raman spectroscopy has not been implemented to investigate the *in situ* changes for CoO_xH_y and NiCoO_xH_y—a class of highly active OER catalysts. Herein, we report the first *operando* Raman spectroscopy study on substoichiometric CoO_xH_y and NiCoO_xH_y catalysts during OER. Using this technique, we present clear evidence of a complex structural evolution that is initiated by an irreversible transformation from a spinel to amorphous CoO structure (spinel → a-CoO), which is followed by a reversible conversion between the amorphous CoO structure and a composite phase consisting of NiOOH motifs in a layered CoO₂ matrix (a-CoO ↔ NiOOH-h-CoO₂). Importantly, incorporation of Ni into CoO_xH_y did not improve its OER activity in the absence of structural evolution during reaction. Our results emphasize the important synergy between catalyst composition and structure, which is required to achieve high OER activity.

■ EXPERIMENTAL METHODS

Synthesis of NiCoO_xH_y by Electrochemical Deposition. CoO_xH_y and NiCoO_xH_y films of different compositions were

synthesized by electrochemical deposition followed by annealing and cyclic voltammetry (CV) treatments. The setup used for the deposition included a working electrode from a fluorine-doped tin oxide substrate (FTO, Aldrich, 7 Ω /sq) and a platinum wire counter electrode. All sample depositions were performed in an aqueous electrolyte containing Co and Ni precursors in different molar ratios. In a typical deposition experiment, the FTO substrate (25 × 16 mm²) was degreased at room temperature with acetone, ethanol, and deionized water for 30 min each. Electrolyte solutions containing 0.1 M Co(NO₃)₂·6H₂O (Aldrich, 99.8%) or a combination of Co(NO₃)₂·6H₂O with Ni(NO₃)₂·6H₂O (Aldrich, 99.999%) were prepared by dissolving the corresponding metal precursors in deionized water. The exposed geometric area for the deposition experiment was 0.97 cm². During deposition, a constant voltage (−2.3 to −2.5 V) was applied to the FTO substrate for 10 min. The resultant films were rinsed with deionized water and allowed to dry in air. Subsequently, the as-deposited films were postprocessed by three methods: (i) the as-deposited films were heated from room temperature to 150 °C and then annealed at 150 °C for 1 h in air, this is referred as the long-time annealing procedure; (ii) the as-deposited samples were placed into the furnace at 100 °C, and then annealed at 150 °C in air for 1 h, this is referred to as the short-time annealing procedure; and (iii) cycling three times using a cyclic voltammetry (CV) protocol from 0 to 0.6 V vs Ag/AgCl at 5 mVs^{−1}. The CV protocol was performed using a three-electrode voltammetry setup, which will be described in a later section. Six samples were investigated in this work. Two samples were prepared by the long-time annealing procedure, and they are denoted as Co-RT and Ni_{4.1}Co-RT. Two samples were prepared by annealing at 150 °C in air for 1 h starting with the furnace preheated to 100 °C in a short-time annealing procedure, and they are denoted as Co-100 and Ni_{5.3}Co-100. Two samples were prepared by the CV cycling procedure, and they are denoted as Co–CV and Ni_{4.2}Co–CV. Subscripts in the sample names represent the surface Ni concentration of the corresponding samples. A NiO_xH_y sample was synthesized by electrodeposition on to a FTO substrate from a 0.1 M Ni(NO₃)₂·6H₂O solution (Aldrich, 99.999%). The as-deposited NiO_xH_y film was treated by the short-time annealing procedure. The synthesis and postprocessing conditions used for each sample are summarized in Table S1.

Materials Characterization of CoO_xH_y and NiCoO_xH_y. Surface morphology of all catalyst films was characterized by scanning electron microscopy (SEM, Quanta 200 FE-SEM). Energy-dispersed X-ray spectroscopy (EDX, Oxford X-Max 20 EDX) was performed to determine Ni distributions in the bulk of the catalyst films. The surface chemical compositions and oxidation states were determined by X-ray photoelectron spectroscopy (XPS, Thermo K-Alpha Plus) with a pass energy of 50 eV and a monochromatized Al K α X-ray source operated at 150 W. XPS binding energies (BE) are reported referenced to the C 1s line at 284.8 eV BE for adventitious carbon.

Electrochemical Characterization of CoO_xH_y and NiCoO_xH_y. OER performance of catalyst films was evaluated using an electrochemical cell with a three-electrode configuration. FTO substrates coated with CoO_xH_y or NiCoO_xH_y catalysts of different compositions were used as working electrodes. A Pt wire (Pine Research Instrument, AFCTR5) was used as a counter electrode, and a double junction Ag/AgCl electrode (Pine Research Instrument, RREF0024) was

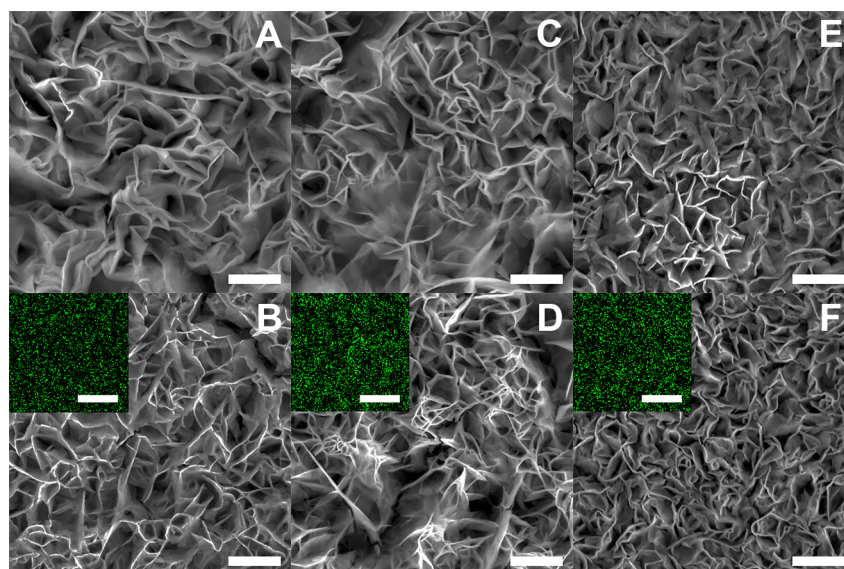


Figure 1. SEM images of catalyst films showing flake-like morphologies at the nanoscale for several samples: (A) Co-RT, (B) $\text{Ni}_{4.1}\text{Co-RT}$, (C) Co-100, (D) $\text{Ni}_{5.3}\text{Co-100}$, (E) Co-CV, and (F) $\text{Ni}_{4.2}\text{Co-CV}$. Scale bars correspond to 1 μm . Insets provide EDX mapping images of Ni distribution in the corresponding catalyst films. Inset scale bars correspond to 10 μm .

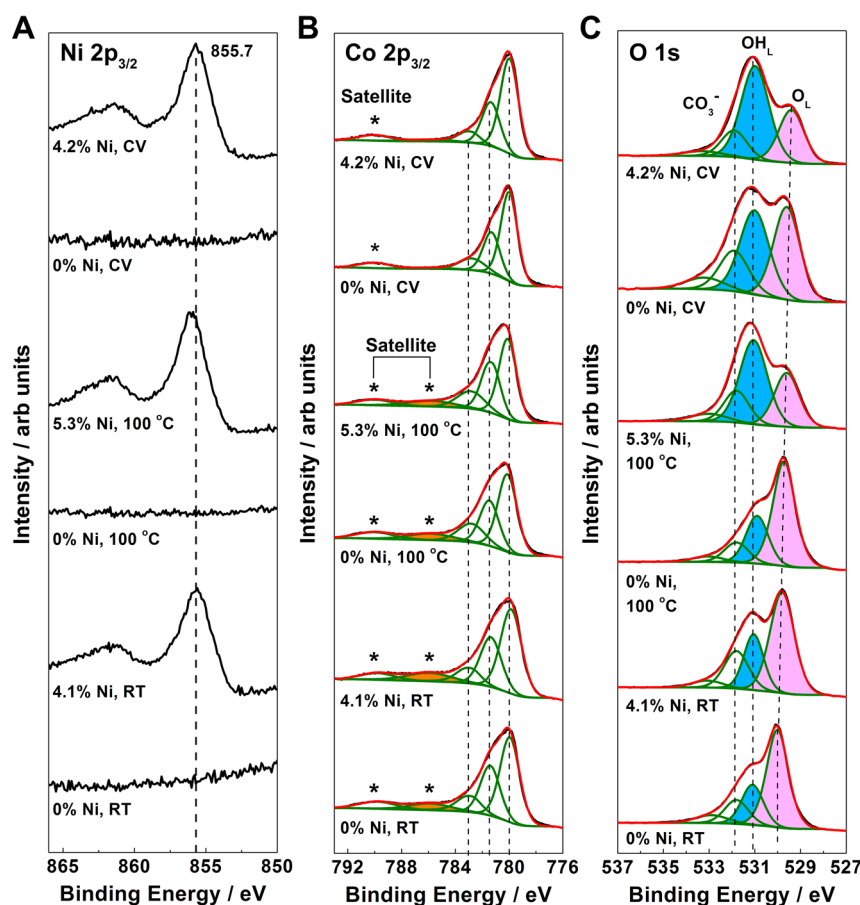


Figure 2. XPS spectra of (A) $\text{Ni } 2p_{3/2}$, (B) $\text{Co } 2p_{3/2}$, and (C) $\text{O } 1s$ regions of CoO_xH_y and NiCoO_xH_y catalyst films.

used as the reference electrode. All three electrodes were connected to a potentiostat (VersaStat 3, Princeton Applied Research). Linear sweep voltammetry (LSV) experiments were conducted in N_2 -saturated 0.1 M KOH from 0 to 1 V vs Ag/AgCl at 1 mVs^{-1} . Uncompensated resistance was determined by electrochemical impedance spectroscopy (EIS), which was

carried out by applying an AC voltage (20 mV peak-to-peak) from 10 kHz to 1 Hz to a working electrode under 0.6 V DC bias. Surface roughness factors were determined by measuring catalyst double layer capacitance in N_2 -saturated 0.1 M KOH from -0.025 to 0.025 V vs open circuit potential at different scan rates (50 to 400 mVs^{-1}). The same three-electrode system

was also used to perform the CV postprocessing for one NiCoO_xH_y sample.

Operando Raman Spectroscopy of CoO_xH_y and NiCoO_xH_y during Reaction. A custom-made electrochemical cell was used for *operando* Raman spectroscopy experiments (Figure S1). In a typical experiment, a FTO substrate coated with a catalyst was used as the working electrode. A platinum wire (Pine Research Instrument, AFCTRS) and an Ag/AgCl electrode (Bioanalytical Systems Incorporation, MF-2021) served as the counter and reference electrodes, respectively. A potentiostat (Pine Research Instrument, WaveNow) was used to apply potentials to the working electrode while Raman spectra were being acquired. A confocal Raman microscope (Horiba, LabRAM Aramis) was used to acquire *in situ* and *operando* Raman spectra using a 533 nm laser (with the power reduced to 0.6 mW) with an acquisition time of 16 s for each spectrum.

RESULTS AND DISCUSSION

Catalyst Morphology and Elemental Composition.

Scanning electron microscopy (SEM) was used to characterize the morphology of catalyst films after different postprocessing treatments. All catalyst films displayed flake-like features at the nanoscale as shown in Figure 1. Ni incorporation and the different postprocessing treatments did not significantly alter the catalyst morphology. The thicknesses of the nanoflakes were similar for all catalysts, however the CV-cycled samples contained visibly smaller size pores (Figure 1E,F). Based on EDX mapping of the catalysts, the distribution of Ni ions in all NiCoO_xH_y samples were uniform (Insets of Figure 1). A uniform distribution of dopant ions has been reported to benefit the OER activity of mixed metal oxides and oxyhydroxides.^{38,39}

XPS was performed on the catalysts to determine their elemental composition, which is summarized in Table S2. The surface Ni concentration depended on the deposition voltage and postprocessing conditions, where a less cathodic potential and shorter annealing duration (directly from 100 °C) favored greater surface Ni concentration in the samples. The local chemical states of surface Ni can be determined by analysis of the Ni $2p_{3/2}$ XPS region, as shown in Figure 2A. The peak position and line shape of the Ni $2p_{3/2}$ spectra are strongly influenced by the oxidation state of Ni and its local structure. For the NiCoO_xH_y catalysts, the principle peak was located at 855.7 eV. This peak position and the broad line shape closely match the Ni $2p_{3/2}$ spectra of Ni(OH)_2 ,^{40,41} which is in contrast to the higher BE of the principle peak position reported for β - NiOOH (855.7–856 eV).^{40,41} Based on these results, divalent Ni ions (Ni^{2+}) are dominant for the $\text{Ni}_{5.1}\text{Co-100}$ and $\text{Ni}_{4.2}\text{Co-CV}$ samples. We ruled out the formation of NiO because its principle peak locates at 853.7 eV BE,^{40–42} and this was not observed in any NiCoO_xH_y samples.

Local chemical states of Co were also investigated using XPS, and the results are shown in Figure 2B. The Co $2p_{3/2}$ XPS spectra of CoO_xH_y and NiCoO_xH_y catalysts were decomposed into five components in accord with the paper by Biesinger et al.⁴³ Based on the line shape of the large peak in the Co $2p_{3/2}$ spectra and the presence of two satellite shakeup features at 786.3 and 790.3 eV in Figure 2B, all catalyst samples annealed at 150 °C contained divalent Co (Co^{2+}) and trivalent Co (Co^{3+}) ions. For the Co-CV and $\text{Ni}_{4.2}\text{Co-CV}$ samples, the absence of a satellite feature at 786.3 eV indicates Co^{3+} is dominant at the catalyst surface. The O 1s spectra of CoO_xH_y

and NiCoO_xH_y catalysts indicate different dominant oxygen species depending on the postprocessing conditions, as shown in Figure 2C. The $\text{OH}_\text{L}/\text{O}_\text{L}$ ratio, where OH_L and O_L denote lattice-OH and lattice-O species, respectively, is less than unity for the Co-RT and $\text{Ni}_{4.1}\text{Co-RT}$ samples. This is indicative of a hydrous oxide (i.e., NiCoO(OH)) structure in the near-surface region (ca. 5 nm). For the short-time annealed and CV-cycled samples, the $\text{OH}_\text{L}/\text{O}_\text{L}$ ratio is greater than unity, which suggests extensive hydroxylation near the catalyst surface and the formation of substoichiometric NiCoO_xH_y . A shift in the O 1s peak from O_L species was observed with Ni incorporation. This can be caused by greater charge transfer from Ni to O_L , which would increase the electron density around O_L and cause a concomitant shift in the peak position toward lower BE. This interaction is especially prevalent in alkali metal oxides where extensive charge transfer to O_L causes a shift in the O 1s peak to lower BE.⁴⁴

Initial Local Structure of CoO_xH_y and NiCoO_xH_y . The local crystal structures of the CoO_xH_y and NiCoO_xH_y samples were investigated by Raman spectroscopy under dry conditions as shown in Figure 3. For the samples subjected to annealing at

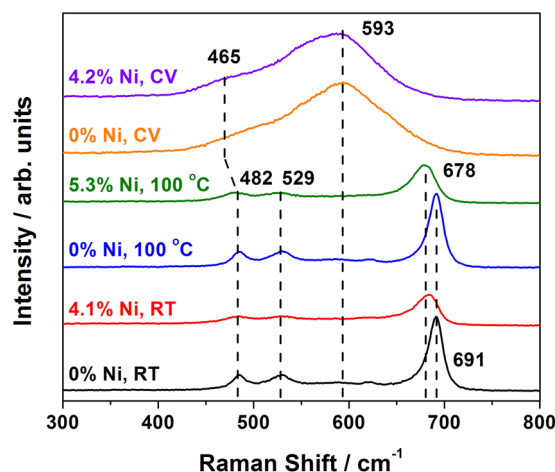


Figure 3. Raman spectra of CoO_xH_y and NiCoO_xH_y catalyst films in dry conditions prior to OER testing.

150 °C, Raman spectra contained three bands at 487, 529, and 698 cm^{-1} , which can be attributed to the Raman-active E_g , $\text{F}_{2\text{g}}$, and $\text{A}_{1\text{g}}$ modes of spinel Co_3O_4 , respectively.⁴⁵ This initial assessment indicated a local spinel structure for all annealed samples. In a spinel structure, both Co^{2+} and Co^{3+} ions are present and they occupy the tetrahedral and octahedral sites, respectively. The E_g and $\text{F}_{2\text{g}}$ vibrations of the spinel lattice are due to both Co^{2+} and Co^{3+} ions, whereas the octahedrally coordinated Co^{3+} ions contribute solely to the strong $\text{A}_{1\text{g}}$ Raman band.⁴⁵ The attenuation, redshift, and broadening of the $\text{A}_{1\text{g}}$ mode suggest local distortions of the CoO_6 octahedra as a result of Ni incorporation. Similar observations have been reported after Fe, Mn, or Zn doping into the Co_3O_4 lattice.^{46,47} In contrast, the Raman spectra of the Co-CV and $\text{Ni}_{4.2}\text{Co-CV}$ catalyst films illustrate a lack of local crystallinity, as indicated by the poorly resolved shoulder and broad Raman band observed for these samples at 465 and 593 cm^{-1} , respectively. We attribute the broad Raman band at 593 cm^{-1} to amorphous CoO_x .^{48–50} The poorly resolved shoulder at 465 cm^{-1} can be attributed to several species, such as CoO_2 in a hexagonal delafossite structure,^{51,52} or the formation of β - and γ -

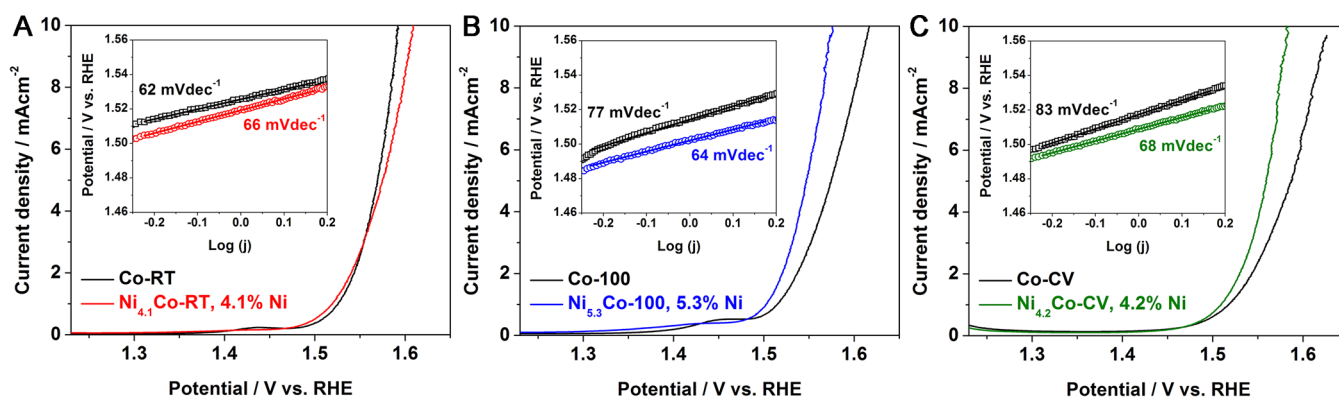


Figure 4. Linear sweep voltammograms of catalyst samples (A) annealed to 150 °C from room temperature, (B) annealed to 150 °C from 100 °C, and (C) CV-cycled. Insets show the corresponding Tafel plots of the corresponding catalysts and their Tafel slope values.

NiOOH.²² Overall, the CV-cycled catalyst films lack long-range order and are considered amorphous based on the broad Raman bands.

Electrochemical OER Performance of Catalyst Films.

Electrochemical measurements using linear sweep voltammetry (LSV), corrected for ohmic losses, were performed to investigate the influence of Ni concentration and postprocessing conditions on the OER activity of CoO_xH_y and NiCoO_xH_y catalyst films, as shown in Figure 4. According to the LSV results, Ni incorporation (4.1 at% Ni) did not improve the OER activity of catalysts that were prepared by longer time annealing (Figure 4A). This observation would seem to suggest that Ni incorporation into a local spinel structure is ineffective for enhancing the OER activity. However, Ni incorporation (5.3 at% Ni) into a catalyst prepared by shorter time annealing led to higher OER activity, despite this catalyst having the same spinel structure (Figure 4B). For the $\text{Ni}_{5.3}\text{Co-100}$ sample that has a 5.3 at% surface Ni concentration, the current density at 0.35 V overpotential was increased by 90% compared to the unmodified catalyst. Despite the same local spinel structure, the influence of Ni on the OER activity of catalysts processed by different annealing conditions was distinct. Interestingly, Ni modification (4.2 at% Ni) of a catalyst having an amorphous structure also improved the OER activity. Compared to the unmodified catalyst, the $\text{Ni}_{4.2}\text{Co-CV}$ sample demonstrated an increase in the current density by 100% at 0.35 V overpotential. All six samples have similar electrode roughness factors based on the double-layer capacitance measurements given in (Figure S2).⁵³ As a result, a difference in surface area is not responsible for the greater OER activities of $\text{Ni}_{5.3}\text{Co-100}$ and $\text{Ni}_{4.2}\text{Co-CV}$ compared to the unmodified catalysts. Incidental Fe incorporation has been reported to affect the OER activity of Ni- and Co-based oxides.^{39,54} To reduce the influence of Fe in the observed activity improvement, we have scavenged Fe ions in the electrolyte solution following the procedures outlined by Burke et al.⁵⁴ The OER activity of Co-100 and $\text{Ni}_{5.3}\text{Co-100}$ tested in Fe-sequestered and unpurified electrolyte solutions were similar, which suggested any Fe incorporation into the catalyst from the electrolyte did not strongly influence the OER activity (Figure S3). Trace amounts of Fe can still be present in the catalyst and affect the catalyst activity; however, this is not the sole reason for the activity improvement we observed for $\text{Ni}_{5.3}\text{Co-100}$ and $\text{Ni}_{4.2}\text{Co-CV}$ based on their higher OER activity compared to the control sample NiO_xH_y (Figure S4). Additional measurements from duplicate samples of each catalyst demonstrated that the improved OER activity as a

result of Ni incorporation and active structure formation is significant (Figure S5). Summarizing the results from LSV experiments and Raman spectroscopy, there is no clear correlation between the surface Ni concentration or catalyst local structure and OER activity. A possible explanation is that the initial structure to which we correlate the OER activities is not an accurate description of the active catalyst phase during reaction. Indeed, structural evolution of cobalt-based oxides that led to the formation of $\text{CoO}(\text{OH})$ during OER has been reported by several groups.^{20,24,26,27,55,56} The situation is more complicated in the case of NiCoO_xH_y catalysts since straightforward predictions are not possible regarding whether the Ni- or Co-containing components, or both, will undergo structural change during OER.

Operando Raman Spectroscopy of Co-RT and $\text{Ni}_{4.1}\text{Co-RT}$ Catalyst Films. We first compared the Raman spectra of the Co-RT and $\text{Ni}_{4.1}\text{Co-RT}$ samples, which showed similar OER activities despite having different Ni concentrations. For the Co-RT catalyst, significant decreases of the intensities of Raman peaks were observed with increasing applied potentials, with the most notable decrease occurring in the A_{1g} Raman band (Figure 5A). Additionally, no shifts in the Raman band positions or the appearance of new features were observed under the entire potential range examined. The Raman band intensities were partially recovered when the applied potentials were reduced to below 0.2 V, which we have assigned as the resting state. As a result, the impact of applied potential on the local spinel structure is partially reversible. We note that the attenuation of the Raman bands was not due to the formation of gas bubbles, based on comparing the optical images of the sample before and after collecting each Raman spectrum.

The A_{1g} Raman band of a spinel structure is associated with the Co–O vibration of CoO_6 octahedra. The substantial decrease in intensity of this A_{1g} band that we observed suggests extensive distortion of the Co–O bonding in the CoO_6 octahedra prior to oxygen evolution. A partial recovery of the A_{1g} band intensity at low applied potentials indicates a reorganization of CoO_6 octahedra in the resting state. Using in situ grazing incidence X-ray diffraction (GIXD), Bergmann et al. observed no change in the spinel structure of the bulk of a Co_3O_4 film over a wide potential window,⁵⁶ which is consistent with our *operando* Raman spectra. Additionally, these authors also found a reversible amorphization of the outermost catalyst surface that resulted in the formation of $\text{CoO}_x(\text{OH})_y$ under OER conditions.⁵⁶ Our Raman approach lacks the surface sensitivity to detect such reversible amorphization in the

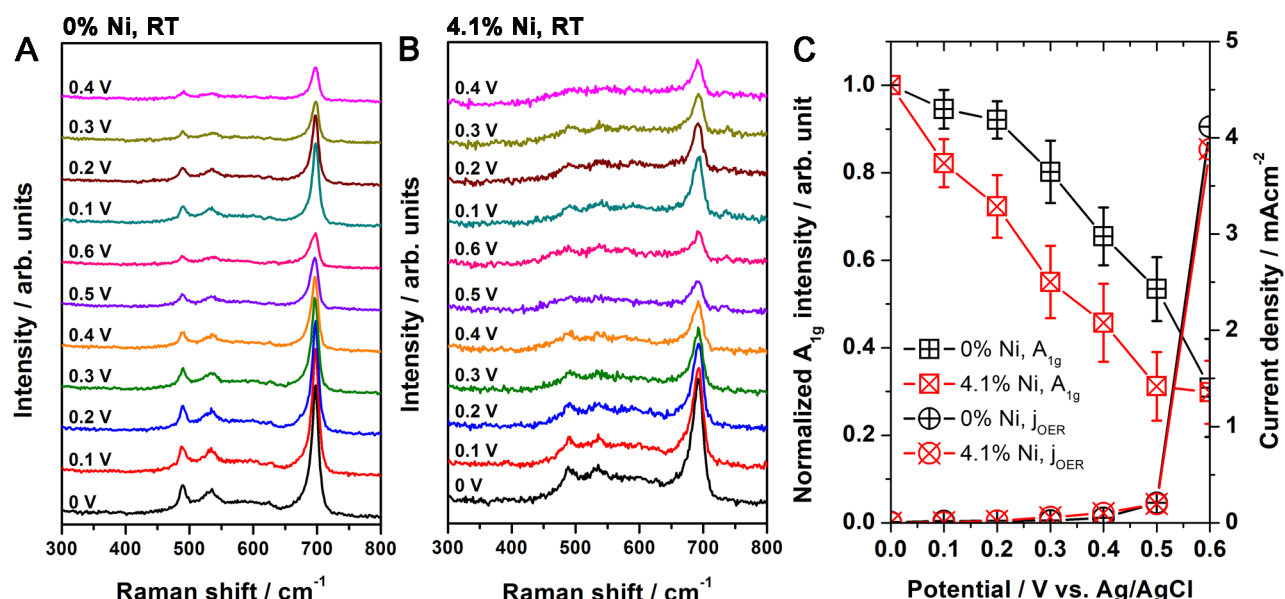


Figure 5. Raman spectra of (A) Co-RT and (B) Ni_{4.1}Co-RT catalyst films under different applied potentials vs Ag/AgCl. (C) Changes in the A_{1g} peak intensity and OER current (j_{OER}) for these films at different applied potentials. The A_{1g} peak intensities are normalized to the intensity of the spectrum acquired at 0 V.

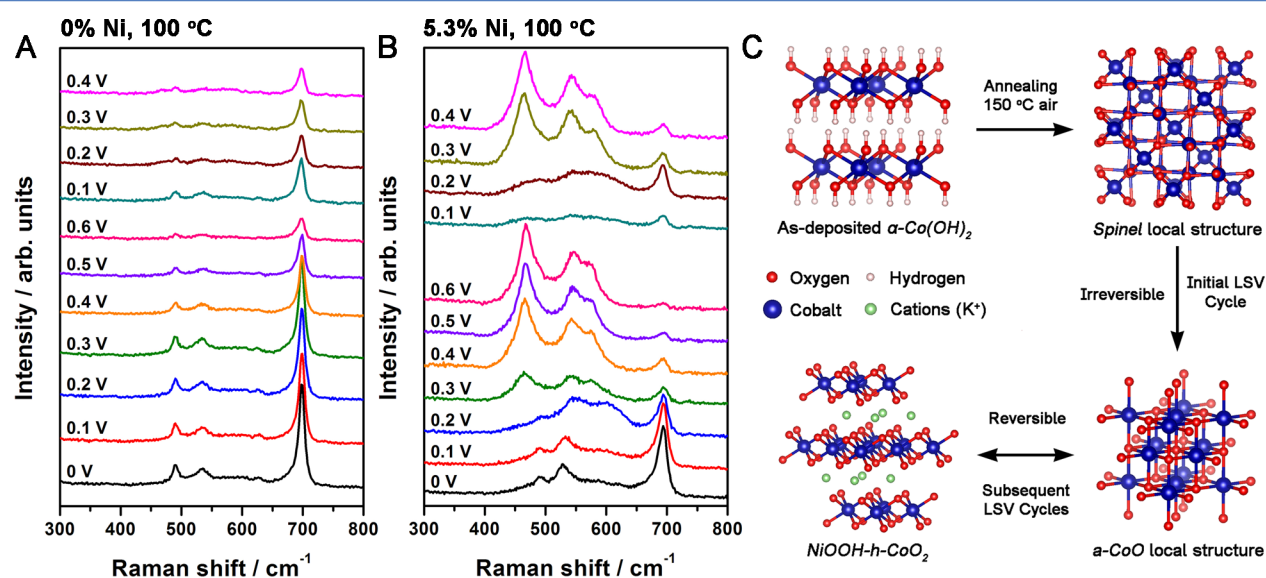


Figure 6. Raman spectra of (A) Co-100 and (B) Ni_{5.3}Co-100 catalyst films under different applied potentials vs Ag/AgCl. (C) Schematic representations of the transformation of Ni_{5.3}Co-100 catalyst films during the OER process based on *operando* Raman results. All as-deposited NiCoO_xH_y films without any postprocessing have a α-Co(OH)₂ local structure based on two characteristic peaks at 453 and 517 cm⁻¹ in the Raman spectra.

outermost layers of the catalyst; however, a similar process likely contributes to the significant, yet partially reversible, changes in our Raman spectra under anodic polarization, as seen in Figure 5A.

Using *in situ* surface-enhanced Raman spectroscopy (SERS), Yeo et al. observed a progressive oxidation of Co₃O₄ to CoO(OH) with increasing anodic potential.²⁴ We did not observe the structural transformation reported by these authors due to the much thicker catalyst films investigated in our study compared to that work (0.4–87 monolayers).²⁴ A recent Raman investigation by Wang et al. reported no attenuation to the Raman active modes of spinel Co₃O₄ during OER, which differs from our observations for our operating catalysts.²¹ We attribute this discrepancy to the different degrees of crystallinity

of the cobalt oxides as a result of different catalyst preparation procedures and the incorporation of Ni. The electrodeposition and low temperature annealing procedures implemented in the synthesis of our catalysts can result in the incorporation of hydroxyl groups and/or water molecules in the bulk of the materials, which can facilitate structural transformation under applied potentials.³⁸ This can be contrasted with procedures involving high temperature annealing of Co₃O₄, as adopted by Wang et al., that generally result in high crystallinity, which can prevent structural change of Co₃O₄.

Raman spectra for the Ni-modified catalyst Ni_{4.1}Co-RT under all anodic potentials investigated, as shown in Figure 5B, were similar to those for the Co-RT samples in Figure 5A. This indicates that Ni incorporation did not alter the catalyst

structure when the $\text{Ni}_{4.1}\text{Co-RT}$ catalyst was prepared by the long-time annealing procedure. The transformation of NiO and $\text{Ni}(\text{OH})_2$ into a catalytically active NiOOH phase prior to oxygen evolution has been observed using in situ XAS^{20,29} and Raman spectroscopy.^{22,25} The absence of Raman bands at 479 and 558 cm^{-1} under high anodic polarization (0.6 V)^{22,25} indicates that Ni incorporation into a spinel lattice prevents the formation of OER-active NiOOH . As expected, we observed similar OER activities for Co-RT and $\text{Ni}_{4.1}\text{Co-RT}$ catalysts films. A monotonic decrease in the A_{1g} Raman band intensity was observed for Co-RT samples at potentials greater than that for the resting state and the structural changes continue at relatively high oxygen evolution rates (ca. 4 mAcm^{-2}), as shown in Figure 5C. For $\text{Ni}_{4.1}\text{Co-RT}$, attenuation of the A_{1g} peak was observed at applied potentials lower than the resting state, and the structural changes did not continue after the onset of oxygen evolution (Figure 5C and Figure S6). Based on the increased attenuation of the A_{1g} band at low applied potentials, Ni incorporation into the spinel lattice caused decreased local crystallinity; however, this was not efficient at promoting OER activity.

Operando Raman Spectroscopy of Co-100 and $\text{Ni}_{5.3}\text{Co-100}$ Catalyst Films. The Co-100 sample exhibited similar structural changes as the Co-RT and $\text{Ni}_{4.1}\text{Co-RT}$ samples, showing only attenuations of the Raman active phonon modes of the spinel structure under anodic polarization, as shown in Figure 6A. However, a very different structural evolution was observed for the $\text{Ni}_{5.3}\text{Co-100}$ sample, as seen in Figure 6B. The local structure for this catalyst at the resting state (0–0.1 V) can be assigned to a local spinel structure based on characteristic phonon modes at 487, 531, and 693 cm^{-1} . Significant structural transformation was observed at 0.2 V, where the A_{1g} band intensity was attenuated and the E_g (487 cm^{-1}) as well as F_{2g} (531 cm^{-1}) modes disappeared. Simultaneously, two broad peaks at 542 and 600 cm^{-1} , as well as a small shoulder at 490 cm^{-1} , appeared. These spectroscopic features in the Raman spectrum obtained at 0.2 V are consistent with the phonon modes of face-centered cubic cobalt oxide (CoO).^{48–50} The Co^{2+} ions in the CoO rock salt structure are octahedrally coordinated and contribute to the A_{1g} Raman active mode at 693 cm^{-1} . The presence of a broad Raman band at 600 cm^{-1} can be attributed to amorphous cobalt oxide according to prior Raman studies.⁴⁹ Utilizing all of these results, we propose an amorphous catalyst structure that contains rock salt CoO motifs (a-CoO) was formed at an applied potential of 0.2 V.

With a further increase in anodic polarization from 0.3 to 0.6 V, substantial structural conversions were observed, as shown in Figure 6B. The Raman band corresponding to the A_{1g} mode was almost eliminated, while two well-defined bands at 467 and 545 cm^{-1} , as well as a poorly resolved shoulder at 577 cm^{-1} , emerged. These three new Raman active bands increased in intensity at greater anodic potentials and can be attributed to the formation of layered CoO_2 and NiOOH . The layered CoO_2 phase is structurally similar to the hexagonal phase of the delafossite structure ($R\bar{3}m$), such as in LiCoO_2 .^{51,52} The Raman spectrum of layered hexagonal LiCoO_2 contains two Raman active modes, E_g at 486 cm^{-1} and A_{1g} at 596 cm^{-1} ,⁵¹ which redshift to 475 and 575 cm^{-1} , respectively, when LiCoO_2 undergoes delithiation.⁵¹ In the case of the $\text{Ni}_{5.3}\text{Co-100}$ films, we expect the samples to contain large concentrations of hydroxyl and/or water molecules in the bulk materials, due to the low temperature synthesis conditions used. The lower

stoichiometry of the $\text{Ni}_{5.3}\text{Co-100}$ sample could be structurally similar to a delithiated LiCoO_2 compound, as indicated by the close agreement of the Raman active band positions. Additionally, the formation of layered hexagonal CoO_2 motifs (h- CoO_2) is consistent with the disappearance of the Raman band at 693 cm^{-1} , which is characteristic of a cubic lattice.

The appearance of Raman bands at 467 and 545 cm^{-1} indicates the formation of NiOOH structural motifs between 0.3 and 0.6 V applied potentials. A progressive oxidation of NiO to $\gamma\text{-NiOOH}$ has been observed prior to oxygen evolution based on the appearance of Raman peaks at 475 and 556 cm^{-1} .²² Similar structural changes involving the conversion of $\text{Ni}(\text{OH})_2/\text{NiO}$ to $\text{Ni}^{(\text{III})}\text{O}(\text{OH})$ was proposed for $(\text{Ni-Fe-Co-Ce})\text{O}_x$ oxide catalysts during oxygen evolution by in situ XAS.²⁰ Our spectroscopic evidence showing Raman bands at 467 and 545 cm^{-1} under high anodic polarization indicates the formation of NiOOH motifs prior to oxygen evolution. As a result, we identify the active local structure of the $\text{Ni}_{5.3}\text{Co-100}$ catalyst film consists of NiOOH motifs in a h- CoO_2 matrix (NiOOH-h-CoO_2) during oxygen evolution. Based on the similar crystal structure of NiOOH motifs and h- CoO_2 , we propose that the formation of large domains of segregated h- CoO_2 and NiOOH is unlikely and that uniform mixing of NiOOH motifs in a h- CoO_2 matrix is the most probable local structure. After reducing the applied potential below 0.2 V, the Raman spectra resemble that of a-CoO. When the catalyst film was placed under relatively high anodic potential (0.4 V), the formation of NiOOH-h-CoO_2 structures was observed again.

Based on these *operando* Raman results, we highlight two important observations on the structural changes of the $\text{Ni}_{5.3}\text{Co-100}$ catalysts under repeated polarization. The initial spinel structure was not recovered after the catalyst was subjected to anodic polarization. Instead, an irreversible transformation from this spinel structure to an amorphous phase containing CoO motifs was observed. Additionally, the transformation between amorphous a-CoO and the OER active NiOOH-h-CoO_2 phase was found to be reversible and was observed exclusively under *operando* conditions. A schematic depiction of the proposed structural evolution is shown in Figure 6C. This sequence of an irreversible transformation of spinel to amorphous a-CoO, followed by a reversible conversion between a-CoO and NiOOH-h-CoO_2 , was observed and reported herein for the first time using *operando* Raman spectroscopy. Trotochaud et al. proposed that in situ formation of layered (oxy)hydroxides from a spinel structure was inhibited; however, its transformation could be possible from an initial rock salt structure after electrochemical conditioning.³⁸ Our *operando* Raman spectroscopy results support this hypothesis and provide additional insight about the structural transformation of Co–Ni metal oxide catalysts. The formation of layered (oxy)hydroxide structures was not observed for the Co-RT and $\text{Ni}_{4.1}\text{Co-RT}$ catalysts that have spinel structures, which is consistent with the hypothesis by Trotochaud et al. However, a transformation of a spinel to layered (oxy)hydroxide structure could be achieved when an intermediary a-CoO structure was involved as demonstrated for the $\text{Ni}_{5.3}\text{Co-100}$ sample (Figure 6C). Additionally, no structural changes occurred for the Co-100 catalyst, which does not contain Ni, indicating that Ni incorporation is necessary to initiate the spinel to a-CoO transformation and to enable subsequent formation of NiOOH-h-CoO_2 . Tung et al. designed an OER-active $\text{Co}_3\text{O}_4@\text{CoO}$ core–shell catalyst and attributed the higher activity of this catalyst over the Co_3O_4 nanoparticles

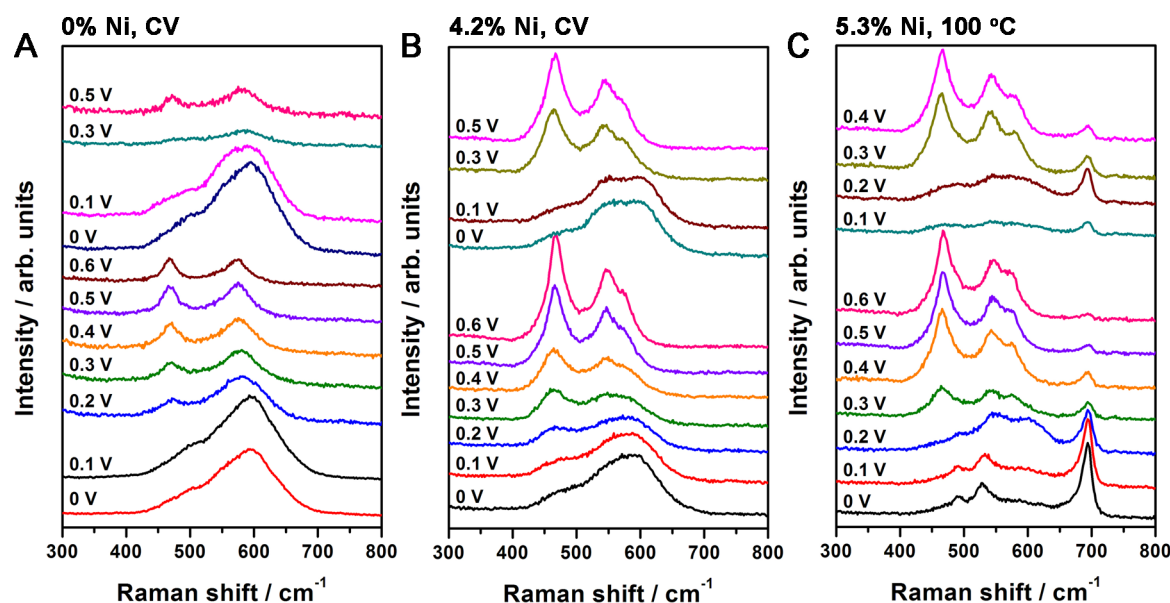


Figure 7. Raman spectra of (A) Co-CV, (B) $\text{Ni}_{4.2}\text{Co}$ -CV, and (C) $\text{Ni}_{5.3}\text{Co}$ -100 catalyst films under different applied potentials.

to the adaptive CoO shell.²⁷ The structural transformation observed by our *operando* Raman spectroscopy results, i.e., $\text{spinel} \rightarrow \text{a-CoO} \leftrightarrow \text{NiOOH-h-CoO}_2$, is in excellent agreement with the results from Tung et al., where the a-CoO phase serves as an adaptive layer to mediate the reversible structural transformation.

We develop several important insights about the structure–activity correlations of Ni-modified CoO_xH_y catalysts by considering the Raman and LSV results together. Ni modification of the Co-100 catalyst prepared by the short-time annealing procedure ($\text{Ni}_{5.3}\text{Co}$ -100) had enhanced OER activity. This increase in activity was accompanied by a substantial structural conversion during OER, which resulted in the formation of an active NiOOH-h-CoO_2 phase having primarily a layered structure. In contrast, Ni modification of the Co-RT catalyst prepared by the long-time annealing procedure ($\text{Ni}_{4.1}\text{Co}$ -RT) did not improve OER activity. Additionally, the initial spinel structure was not altered by Ni incorporation and a structural transformation during OER was not observed. On the basis of these observations, Ni incorporation in a spinel lattice does not improve the OER activity of CoO_xH_y catalysts, whereas Ni incorporation in a layered structure is effective for enhancing catalyst activity. Furthermore, we proposed that the active structure of NiCoO_xH_y samples prepared by annealing was an amalgamation of NiOOH -like motifs in a layered hexagonal CoO_2 matrix. These results emphasize the important synergy between catalyst composition and structure; i.e., Ni needs to be in a specific local environment to effectively promote the OER activity of CoO_xH_y catalysts. We also performed *operando* Raman spectroscopy on NiO_xH_y samples prepared using the same short-time annealing procedure. Consistent with reported literature results, the NiO_xH_y catalyst underwent an irreversible structural change with anodic polarization and formed NiOOH during OER (Figure S4C), which is a component of the active phase we observed for $\text{Ni}_{5.3}\text{Co}$ -100 samples. Comparing the OER performance of NiO_xH_y and $\text{Ni}_{5.3}\text{Co}$ -100 catalysts, both samples demonstrated similar current density at $\eta = 0.35$ V. However, better kinetics was observed for $\text{Ni}_{5.3}\text{Co}$ -100 catalysts compared to NiO_xH_y catalysts at $\eta = 0.35$ V. As a result, the active-phase structure

reported here, i.e., NiOOH-h-CoO_2 , has greater OER activity than that of NiOOH by itself. This is strong support for a synergistic effect of Ni incorporation in improving the OER activity of CoO_xH_y catalysts.

Operando Raman Spectroscopy of Co-CV and $\text{Ni}_{4.2}\text{Co}$ -CV Catalyst Films. The CoO_xH_y and NiCoO_xH_y catalysts we have discussed thus far all have an initial spinel structure. A priori it is unclear whether different initial structures will result in the formation of different active phases. To study this, we examined during OER the Raman spectra of catalysts synthesized using a CV cycling procedure. These results are shown in Figure 7. At low anodic potentials, the Co-CV sample was highly amorphous as indicated by the broad Raman band at 590 cm^{-1} . With increasing anodic polarization to 0.6 V, two well-defined Raman bands appeared at 467 and 572 cm^{-1} , which correspond to the E_g and A_{1g} modes, respectively, of layered hexagonal CoO_2 . Repeated anodic polarization confirmed that the conversion from an amorphous phase to an OER-active h- CoO_2 structure was reversible. LiCoO_2 is a closely related oxide having a local structure similar to the h- CoO_2 that is formed during OER. LiCoO_2 has two polymorphs with cubic and hexagonal structures.^{51,52,57} The hexagonal phase of stoichiometric and delithiated LiCoO_2 have Raman spectra similar to h- CoO_2 and have been demonstrated to be active for OER.^{57–59} Thus, our assignment that h- CoO_2 is the OER-active phase of our CoO_xH_y catalysts is consistent with previous reports in the literature.

Similar to the unmodified Co-CV samples, the $\text{Ni}_{4.2}\text{Co}$ -CV catalyst is also amorphous under low applied potentials. With increasing anodic potentials, the formation of a NiOOH-h-CoO_2 structure was observed as characterized by the well-defined Raman bands at 467 and 547 cm^{-1} , as well as a shoulder at 575 cm^{-1} . Compared to the annealed samples, as shown in Figure 7C, the $\text{Ni}_{4.2}\text{Co}$ -CV sample did not show an initial irreversible structure change, but the same active structure was formed that also demonstrated good reversibility. This conclusion is critical as it highlights the formation of a unique active phase during OER for these CoO_xH_y catalysts showing initially lower crystallinity. Further support for our

hypothesis that NiOOH-h-CoO₂ is the OER active structure is provided by the better OER performance of the Ni₄Co-CV catalyst compared to the Co-CV catalyst. Additionally, although the formation of the NiOOH-h-CoO₂ active structure is independent of the initial cobalt oxide catalyst structures, the presence of Ni in the catalyst is still required.

CONCLUSION

In conclusion, we have observed for the first time the formation of an unique OER-active structure for NiCoO_xH_y catalysts in which the catalyst films transformed from spinel to amorphous a-CoO and then to the OER-active structure NiOOH-h-CoO₂ at 0.2 and 0.3 V vs Ag/AgCl, respectively. The initial transformation from spinel to a-CoO structure is irreversible; however, the subsequent conversion to NiOOH-h-CoO₂ is reversible. A short catalyst annealing duration and the incorporation of Ni were necessary to initiate the irreversible transformation process that is required for the subsequent formation of the active structure, which is an amalgamation of NiOOH motifs and layered hexagonal CoO₂. Incorporation of Ni into this active structure is necessary to improve the OER activity of NiCoO_xH_y catalysts, which was increased by 100% compared to when Ni was coordinated in a spinel structure. Furthermore, the same active structure is formed, independent of the initial cobalt oxide catalyst structure, which indicates that the NiOOH-h-CoO₂ structure can be an universal OER-active structure for NiCoO_xH_y catalysts.

ASSOCIATED CONTENT

Supporting Information

The Supporting Information is available free of charge on the ACS Publications website at DOI: 10.1021/acscatal.7b03191.

Schematic of *operando* Raman cell; surface roughness factor of catalysts; OER activity of catalyst in Fe-purified electrolyte; OER activity and *operando* Raman spectroscopy of NiO_xH_y; catalyst stability in alkaline conditions; synthesis conditions and processing treatments (PDF)

AUTHOR INFORMATION

Corresponding Authors

*E-mail: bkoel@princeton.edu

*E-mail: shshen_xjtu@mail.xjtu.edu.cn.

ORCID

Liejun Guo: 0000-0002-3671-5628

Bruce E. Koel: 0000-0002-0032-4991

Author Contributions

[†]Z.C. and L.C. contributed equally to this work.

Notes

The authors declare no competing financial interest.

ACKNOWLEDGMENTS

This research is based upon work supported by the National Science Foundation under Grant No. CHE-1465082. Z.C. acknowledges support from the Maeder Graduate Fellowship of the Andlinger Center for Energy and the Environment at Princeton University. L.C. acknowledges support from the National Natural Science Foundation of China (Nos. 51678810, 51323011).

REFERENCES

- (1) Zhang, L. X.; Zhang, S. L.; Zhang, K. J.; Xu, G. J.; He, X.; Dong, S. M.; Liu, Z. H.; Huang, C. S.; Gu, L.; Cui, G. L. *Chem. Commun.* **2013**, 49, 3540–3542.
- (2) Wang, Z. L.; Xu, D.; Xu, J. J.; Zhang, X. B. *Chem. Soc. Rev.* **2014**, 43, 7746–7786.
- (3) Inoue, H.; Shimada, T.; Kou, Y.; Nabetani, Y.; Masui, D.; Takagi, S.; Tachibana, H. *ChemSusChem* **2011**, 4, 173–179.
- (4) Marini, S.; Salvi, P.; Nelli, P.; Pesenti, R.; Villa, M.; Berrettoni, M.; Zangari, G.; Kirov, Y. *Electrochim. Acta* **2012**, 82, 384–391.
- (5) Song, S. D.; Zhang, H. M.; Ma, X. P.; Shao, Z. G.; Baker, R. T.; Yi, B. L. *Int. J. Hydrogen Energy* **2008**, 33, 4955–4961.
- (6) Suntivich, J.; May, K. J.; Gasteiger, H. A.; Goodenough, J. B.; Shao-Horn, Y. *Science* **2011**, 334, 1383–1385.
- (7) Chen, G. Y.; Bare, S. R.; Mallouk, T. E. *J. Electrochem. Soc.* **2002**, 149, A1092–A1099.
- (8) Fabbri, E.; Haberer, A.; Waltar, K.; Kotz, R.; Schmidt, T. J. *Catal. Sci. Technol.* **2014**, 4, 3800–3821.
- (9) Kotz, R.; Stucki, S.; Scherson, D.; Kolb, D. M. *J. Electroanal. Chem. Interfacial Electrochem.* **1984**, 172, 211–219.
- (10) Rogers, D. B.; Shannon, R. D.; Sleight, A. W.; Gillson, J. L. *Inorg. Chem.* **1969**, 8, 841–849.
- (11) Seitz, L. C.; Dickens, C. F.; Nishio, K.; Hikita, Y.; Montoya, J.; Doyle, A.; Kirk, C.; Vojvodic, A.; Hwang, H. Y.; Nørskov, J. K.; Jaramillo, T. F. *Science* **2016**, 353, 1011–1014.
- (12) Reier, T.; Oezaslan, M.; Strasser, P. *ACS Catal.* **2012**, 2, 1765–1772.
- (13) Lee, Y.; Suntivich, J.; May, K. J.; Perry, E. E.; Shao-Horn, Y. *J. Phys. Chem. Lett.* **2012**, 3, 399–404.
- (14) Johnson, B.; Girgsdies, F.; Weinberg, G.; Rosenthal, D.; Knop-Gericke, A.; Schlögl, R.; Reier, T.; Strasser, P. *J. Phys. Chem. C* **2013**, 117, 25443–25450.
- (15) Gorlin, Y.; Chung, C. J.; Benck, J. D.; Nordlund, D.; Seitz, L.; Weng, T. C.; Sokaras, D.; Clemens, B. M.; Jaramillo, T. F. *J. Am. Chem. Soc.* **2014**, 136, 4920–4926.
- (16) Gorlin, Y.; Jaramillo, T. F. *J. Am. Chem. Soc.* **2010**, 132, 13612–13614.
- (17) McCrory, C. C. L.; Jung, S.; Ferrer, I. M.; Chatman, S. M.; Peters, J. C.; Jaramillo, T. F. *J. Am. Chem. Soc.* **2015**, 137, 4347–4357.
- (18) Burke, M. S.; Zou, S. H.; Enman, L. J.; Kellon, J. E.; Gabor, C. A.; Pledger, E.; Boettcher, S. W. *J. Phys. Chem. Lett.* **2015**, 6, 3737–3742.
- (19) Burke, M. S.; Enman, L. J.; Batchellor, A. S.; Zou, S. H.; Boettcher, S. W. *Chem. Mater.* **2015**, 27, 7549–7558.
- (20) Favaro, M.; Drisdell, W. S.; Marcus, M. A.; Gregoire, J. M.; Crumlin, E. J.; Haber, J. A.; Yano, J. *ACS Catal.* **2017**, 7, 1248–1258.
- (21) Wang, H. Y.; Hung, S. F.; Hsu, Y. Y.; Zhang, L. L.; Miao, J. W.; Chan, T. S.; Xiong, Q. H.; Liu, B. *J. Phys. Chem. Lett.* **2016**, 7, 4847–4853.
- (22) Yeo, B. S.; Bell, A. T. *J. Phys. Chem. C* **2012**, 116, 8394–8400.
- (23) Louie, M. W.; Bell, A. T. *J. Am. Chem. Soc.* **2013**, 135, 12329–12337.
- (24) Yeo, B. S.; Bell, A. T. *J. Am. Chem. Soc.* **2011**, 133, 5587–5593.
- (25) Klaus, S.; Cai, Y.; Louie, M. W.; Trotochaud, L.; Bell, A. T. *J. Phys. Chem. C* **2015**, 119, 7243–7254.
- (26) Friebe, D.; Bajdich, M.; Yeo, B. S.; Louie, M. W.; Miller, D. J.; Casalongue, H. S.; Mbuga, F.; Weng, T. C.; Nordlund, D.; Sokaras, D.; Alonso-Mori, R.; Bell, A. T.; Nilsson, A. *Phys. Chem. Chem. Phys.* **2013**, 15, 17460–17467.
- (27) Tung, C. W.; Hsu, Y. Y.; Shen, Y. P.; Zheng, Y. X.; Chan, T. S.; Sheu, H. S.; Cheng, Y. C.; Chen, H. M. *Nat. Commun.* **2015**, 6, 8106.
- (28) Zhang, M.; de Respinis, M.; Frei, H. *Nat. Chem.* **2014**, 6, 362–367.
- (29) Friebe, D.; Louie, M. W.; Bajdich, M.; Sanwald, K. E.; Cai, Y.; Wise, A. M.; Cheng, M. J.; Sokaras, D.; Weng, T. C.; Alonso-Mori, R.; Davis, R. C.; Nørskov, J. K.; Nilsson, A.; Bell, A. T. *J. Am. Chem. Soc.* **2015**, 137, 1305–1313.
- (30) Liang, Y. Y.; Li, Y. G.; Wang, H. L.; Zhou, J. G.; Wang, J.; Regier, T.; Dai, H. *J. Nat. Mater.* **2011**, 10, 780–786.

- (31) Rosen, J.; Hutchings, G. S.; Jiao, F. *J. Am. Chem. Soc.* **2013**, *135*, 4516–4521.
- (32) Chen, Z.; Kronawitter, C. X.; Koel, B. E. *Phys. Chem. Chem. Phys.* **2015**, *17*, 29387–29393.
- (33) He, S.; Huang, Y. Y.; Huang, J. H.; Liu, W.; Yao, T.; Jiang, S.; Tang, F. M.; Liu, J. K.; Hu, F. C.; Pan, Z. Y.; Liu, Q. H. *J. Phys. Chem. C* **2015**, *119*, 26362–26366.
- (34) Huang, J. H.; Chen, J. T.; Yao, T.; He, J. F.; Jiang, S.; Sun, Z. H.; Liu, Q. H.; Cheng, W. R.; Hu, F. C.; Jiang, Y.; Pan, Z. Y.; Wei, S. Q. *Angew. Chem., Int. Ed.* **2015**, *54*, 8722–8727.
- (35) Liang, H. F.; Meng, F.; Caban-Acevedo, M.; Li, L. S.; Forticaux, A.; Xiu, L. C.; Wang, Z. C.; Jin, S. *Nano Lett.* **2015**, *15*, 1421–1427.
- (36) Liu, Y. C.; Koza, J. A.; Switzer, J. A. *Electrochim. Acta* **2014**, *140*, 359–365.
- (37) Liu, H. F.; Patzke, G. R. *Chem. - Asian J.* **2014**, *9*, 2249–2259.
- (38) Trotochaud, L.; Ranney, J. K.; Williams, K. N.; Boettcher, S. W. *J. Am. Chem. Soc.* **2012**, *134*, 17253–17261.
- (39) Trotochaud, L.; Young, S. L.; Ranney, J. K.; Boettcher, S. W. *J. Am. Chem. Soc.* **2014**, *136*, 6744–6753.
- (40) Biesinger, M. C.; Payne, B. P.; Lau, L. W. M.; Gerson, A.; Smart, R. S. *Surf. Interface Anal.* **2009**, *41*, 324–332.
- (41) Grosvenor, A. P.; Biesinger, M. C.; Smart, R. S.; McIntyre, N. S. *Surf. Sci.* **2006**, *600*, 1771–1779.
- (42) Schulze, M.; Reissner, R.; Lorenz, M.; Radke, U.; Schnurnberger, W. *Electrochim. Acta* **1999**, *44*, 3969–3976.
- (43) Biesinger, M. C.; Payne, B. P.; Grosvenor, A. P.; Lau, L. W. M.; Gerson, A. R.; Smart, R. S. *Appl. Surf. Sci.* **2011**, *257*, 2717–2730.
- (44) Dupin, J. C.; Gonbeau, D.; Vinatier, P.; Levasseur, A. *Phys. Chem. Chem. Phys.* **2000**, *2*, 1319–1324.
- (45) Hadjiev, V. G.; Iliev, M. N.; Vergilov, I. V. *J. Phys. C: Solid State Phys.* **1988**, *21*, L199–L201.
- (46) Na, C. W.; Woo, H. S.; Kim, H. J.; Jeong, U.; Chung, J. H.; Lee, J. H. *CrystEngComm* **2012**, *14*, 3737–3741.
- (47) Stella, C.; Soundararajan, N.; Ramachandran, K. *AIP Adv.* **2015**, *5*, 087104.
- (48) Lojewski, J.; Kolodziej, A.; Lojewski, T.; Kapica, R.; Tyczkowski, J. *Appl. Catal., A* **2009**, *366*, 206–211.
- (49) Ravindra, A. V.; Behera, B. C.; Padhan, P. *J. Nanosci. Nanotechnol.* **2014**, *14*, 5591–5595.
- (50) Ravindra, A. V.; Behera, B. C.; Padhan, P.; Lebedev, O. I.; Prellier, W. *J. Appl. Phys.* **2014**, *116*, 033912.
- (51) Inaba, M.; Iriyama, Y.; Ogumi, Z.; Todzuka, Y.; Tasaka, A. *J. Raman Spectrosc.* **1997**, *28*, 613–617.
- (52) Song, S. W.; Han, K. S.; Fujita, H.; Yoshimura, M. *Chem. Phys. Lett.* **2001**, *344*, 299–304.
- (53) Koza, J. A.; He, Z.; Miller, A. S.; Switzer, J. A. *Chem. Mater.* **2012**, *24*, 3567–3573.
- (54) Burke, M. S.; Kast, M. G.; Trotochaud, L.; Smith, A. M.; Boettcher, S. W. *J. Am. Chem. Soc.* **2015**, *137*, 3638–3648.
- (55) Risch, M.; Ringleb, F.; Kohlhoff, M.; Bogdanoff, P.; Chernev, P.; Zaharieva, I.; Dau, H. *Energy Environ. Sci.* **2015**, *8*, 661–674.
- (56) Bergmann, A.; Martinez-Moreno, E.; Teschner, D.; Chernev, P.; Gliech, M.; de Araujo, J. F.; Reier, T.; Dau, H.; Strasser, P. *Nat. Commun.* **2015**, *6*, 8625.
- (57) Gardner, G.; Al-Sharab, J.; Danilovic, N.; Go, Y. B.; Ayers, K.; Greenblatt, M.; Dismukes, G. C. *Energy Environ. Sci.* **2016**, *9*, 184–192.
- (58) Gardner, G. P.; Go, Y. B.; Robinson, D. M.; Smith, P. F.; Hadermann, J.; Abakumov, A.; Greenblatt, M.; Dismukes, G. C. *Angew. Chem., Int. Ed.* **2012**, *51*, 1616–1619.
- (59) Maiyalagan, T.; Jarvis, K. A.; Therese, S.; Ferreira, P. J.; Manthiram, A. *Nat. Commun.* **2014**, *5*, 3949.